



Carbon Corrosion in PEM Fuel Cell Dead-Ended Anode Operations

Jixin Chen,^{*,z} Jason B. Siegel,^{*} Toyooki Matsuura,^{**} and Anna G. Stefanopoulou

Department of Mechanical Engineering, University of Michigan, Ann Arbor, Michigan 48109, USA

This paper investigates the effects of dead-ended anode (DEA) operation on the electrode carbon corrosion of the Proton Exchange Membrane (PEM) fuel cell. A reduced order isothermal model is developed focusing on the species concentration along the channel and associated membrane phase potential. This model explains, and can be used to quantify, the carbon corrosion behavior during DEA operation of a PEM fuel cell. The presence of oxygen in the anode channel, although normally less than 5% in molar fraction, creates a H₂/O₂ front as N₂ and water accumulate at the end of the channel and hydrogen is depleted along the channel. The presence of oxygen in the anode channel also results in a gradual drop of the membrane phase potential, promoting carbon corrosion in the cathode. The corrosion rate is driven by the local species concentration in the anode, which varies in space and time. In a co-flow configuration, the large spatio-temporal patterns of hydrogen starvation in the end of the anode channel induce the highest carbon corrosion, which, in turn, is shown to be moderated by the decreasing terminal voltage during galvanostatic operation. Although not fully calibrated, the model shows good agreement with preliminary *in situ* observations.

© 2011 The Electrochemical Society. [DOI: 10.1149/1.3609770] All rights reserved.

Manuscript submitted March 30, 2011; revised manuscript received June 8, 2011. Published July 20, 2011.

A proton exchange membrane (PEM) fuel cell under dead-ended anode (DEA) condition is fed by dry hydrogen with regulated pressure at the anode inlet.¹⁻³ Inlet pressure regulation ensures that the hydrogen inlet stoichiometry is exactly one during DEA operation and the channel pressure remains constant. This system architecture, shown in Fig. 1b, depends on less auxiliary components when compared to the more traditional operating mode, which employs hydrogen flow control shown in Fig. 1a. The operation with hydrogen flow control depends on a recirculation loop (the RCA in Fig. 1a) to maintain a high hydrogen utilization. The recirculation loop requires hydrogen grade plumbing and hardware such as an ejector/blower, water separator, and hydrogen humidifier. These components add weight, volume, and expense to the system. In the DEA operation, the water crossing through the membrane contributes to humidifying the hydrogen fuel so that anode inlet humidification can be removed or reduced.

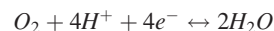
The simplified balance of plant (BOP) in the DEA operation unfortunately comes with a major concern. The accumulation of nitrogen and liquid water in the anode channel during DEA operation may lead to local fuel depletion or starvation, and the associated carbon corrosion in the catalyst layer becomes a problem. This accumulation also causes a gradual, but recoverable, drop in cell voltage over time. When operating in galvanostatic mode, purges are necessary to remove nitrogen/water from the anode and to recover the voltage. This periodic purging event causes voltage cycling in DEA operation, with a cycle defined as the duration between two consecutive purge events. The evolution of the cell voltage and the concentration of the species is very repeatable from cycle to cycle, because liquid water and inert gas accumulate at the end of the vertically oriented straight anode channels.³

The hydrogen flow in a re-circulated anode makes convection a dominant force that determines the variation in channel gas composition. Convection is equally important in the DEA operation^{4,5} despite the very low anode flow rates that have led to the use of the continuous stirred tank reactor (CSTR) methodology in fuel cell with open channels.⁶ When operating with a DEA both convection and diffusion influence the distribution of gasses in the channel. Convection dominates transport at the channel inlet, pushing hydrogen, nitrogen, oxygen and water towards the end of the channel. Gasses and water crossover from the cathode to the anode and accumulate at the end of the anode channel, blocking hydrogen from reaching this region. The hydrogen depleted region grows, reaching back toward the inlet as nitrogen accumulation continues during DEA operation. The presence of oxygen in the end region of the an-

ode channel, where hydrogen is depleted, is of particular concern for cathode carbon corrosion.

The carbon corrosion in the catalyst layer is a major degradation source in operating a PEM fuel cell.^{7,8} The carbon catalyst support in PEM fuel cell is itself thermodynamically unstable due to its low equilibrium potential of 0.207 V with respect to reversible hydrogen electrode (RHE) at 25°C. Fortunately, under typical operating temperature (65°C) and interfacial potential (0.6 V) between membrane phase and metal phase, the carbon corrosion rate is considered negligible.⁹ However, it is also reported that electrocatalysts such as Pt may lower the safe interfacial potential to 0.55 V or lower.¹⁰ Hence the threshold potential may depend on the catalyst performance and operating conditions.

This paper combines various mathematical models necessary for quantifying the carbon corrosion behavior in an operating cell with a DEA. In previous work,^{11,12} a model of the nitrogen blanketing and water plugging effects was developed for DEA operation. The model predicts the fuel depletion observed in the experiments. Fuel depletion in the anode channel not only results in cell voltage decrease but also triggers carbon corrosion. As hydrogen is no longer sufficient to maintain the current (in galvanostatic operation), the equilibrium of



would move backwards due to the lack of hydrogen ions. Thus, at the location of fuel depletion, oxygen could be generated from water dissociation, in addition to the general source of oxygen crossover through membrane. The amount of oxygen in the anode is negligible whenever there is sufficient hydrogen (proton) supply since it would be instantaneously reduced to water. The insufficiency of hydrogen also promotes



although it proceeds at a slower rate compared with water dissociation.

The scenario of carbon corrosion in DEA operation is as follows. As shown in Fig. 2a, initially ($t = t_0$), when hydrogen completely occupies the anode after a purge, the membrane exhibits uniform potential along y direction. The uniform potential is slightly negative ($\sim -0.01V$) as the anode metal potential is zero.

As time evolves ($t = t_1$), hydrogen depletion in the anode occurs (see Fig. 8) due to the nitrogen/oxygen crossover and the water flooding. The presence of oxygen in the anode is crucial, which leads to the membrane phase potential drop in the area of hydrogen depletion. Thus anode and cathode interfacial potentials increase compared with $t = t_0$ (see Fig. 11).

* Electrochemical Society Student Member.

** Electrochemical Society Active Member.

^z E-mail: jixinc@umich.edu

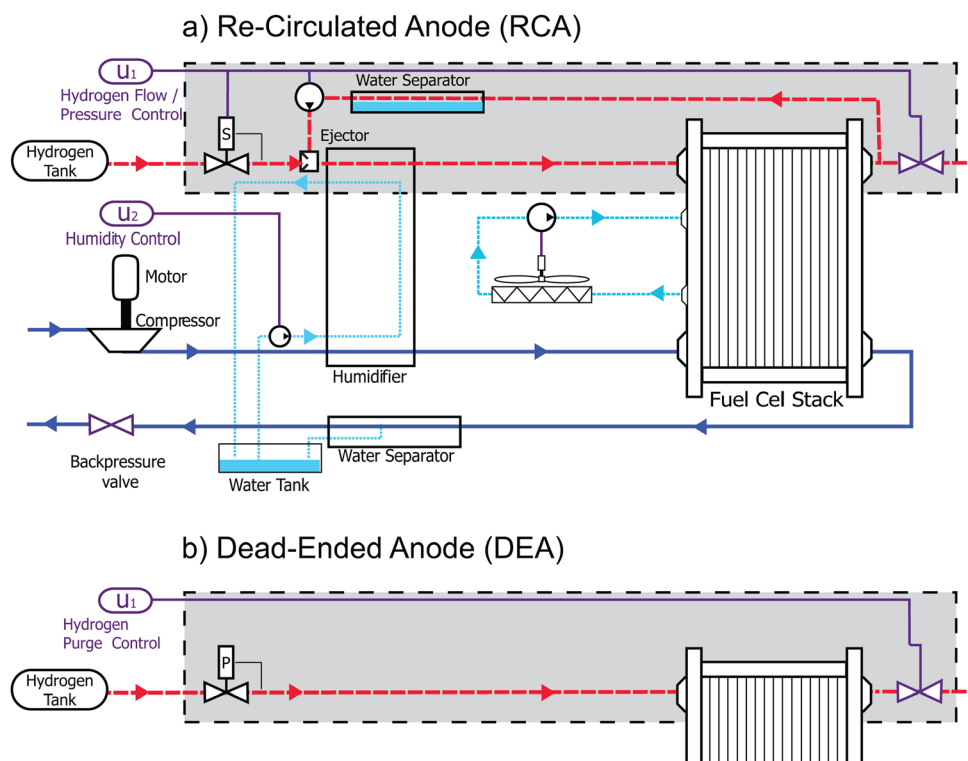


Figure 1. (Color online) Schematic of fuel cell systems with anode re-circulation versus dead-ended anode. DEA operation features upstream pressure regulation instead of mass flow control and removal of re-circulation and hydrogen humidification systems.

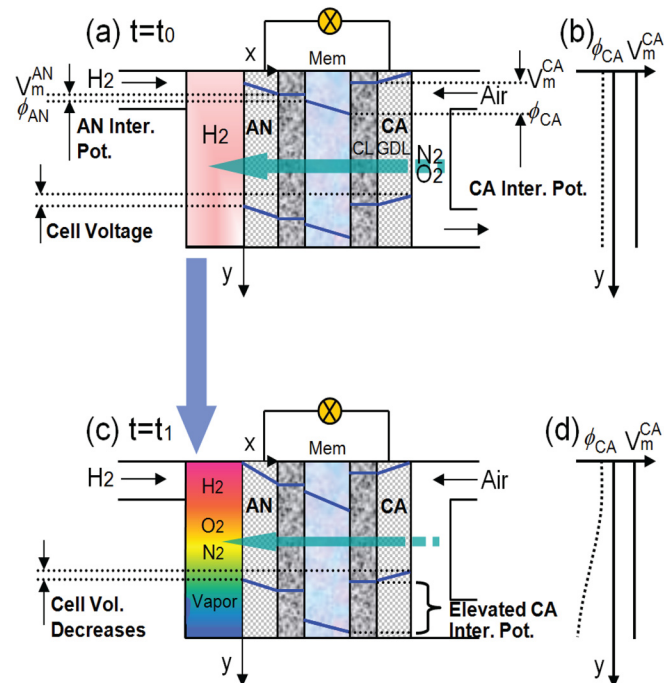


Figure 2. (Color online) Scenario of carbon corrosion in DEA operation (not to scale). Subfigure (a) Shows the initial reactant distribution (uniform hydrogen) immediately after an anode purge. Subfigure (c) shows the reactant distribution and resulting change in interfacial potential at the end of the channels right before an anode purge. Subfigures (b) and (d) are the cathode membrane/metal phase potentials corresponding to subfigures (a) and (c), respectively. The differences between V_m^{AN} and ϕ_{AN} , V_m^{CA} and ϕ_{CA} are termed interfacial potentials at anode and cathode, respectively. The magnitude of interfacial potential directly determines the carbon corrosion rate. The difference between V_m^{CA} and V_m^{AN} is the cell voltage.

A special case of carbon corrosion caused by the development of a H_2/O_2 boundary in the anode that occurs during the start-up/shutdown process of the cell has been studied both numerically^{9,13,14} and experimentally.¹⁵⁻¹⁹ The corrosion mechanism for this case can be illustrated by Fig. 3, where the dotted line indicates the H_2/O_2 boundary. In this case, the complete hydrogen starvation in the rear part of the anode channel leads to high interfacial potential ($\sim 1.6V$) at the cathode. The cathode carbon can be completely oxidized within hours under such potential. Start-up/shutdown procedures have been proposed to alleviate such carbon corrosion issues.^{20,21}

In this paper we employ a 1-D along-channel model to study DEA operation. Multi-dimensional modeling is not necessary to capture the observed voltage behavior due to the along-channel stratified patterns.²² A carbon corrosion model is developed based on the corrosion mechanism in Ref. 23 and then incorporated into our prior model which predicts the nitrogen accumulation.¹¹ The important parameter to capture by modeling is the oxygen concentration in the anode, and the associated current density of each reaction. In the following section, the model equations are presented and discussed. The model is then validated in Model Parameterization section with simulation results discussed in Simulation Results section.

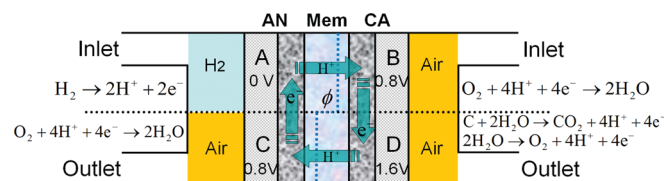


Figure 3. (Color online) Schematic of the carbon corrosion mechanism due to the clear H_2/O_2 boundary, which usually forms during start-up/shutdown of the cell.^{9,15}

Model Equations

In DEA operation diffusion prevents the development of a sharp interface between fuel and oxidant in the anode channel, which is different from the start-up/shutdown case with H_2/O_2 boundary. Nitrogen, oxygen and water can cross through the membrane in either direction, however the convective flux due to hydrogen consumption causes the accumulation of inert and product gasses at the end of the channel.

With these features and other simplifications, the major assumptions in the present model are: (1) the model is simplified to one dimension along the channel direction. (2) The effects of liquid water are not considered in the model. (3) The electrochemical loss of Pt (Refs. 24 and 25) is not modeled. The particle size of Pt and formation of PtO layer affect the carbon reaction rate, but we control the cell potential in both simulation and experiments to avoid high interfacial potential (< 1.2 V) at cathode, thus the electrochemical loss of Pt is minimized. The loss of active Pt sites, however, is reflected in the present model via a correlation with the remaining carbon in the catalyst layer. (4) The membrane degradation, such as chemical decomposition of the polymer, also contributes to the cell voltage decay.^{26–28} The present model assumes a good membrane condition. (5) We consider only the carbon corrosion in the catalyst layer, and do not include any impacts from the instability of the GDL material.⁸

There are six dynamic states in the model: the molar fractions of N_2 , O_2 and vapor ($n_{N_2,O_2,V}$) in the anode channel, the partial pressure of O_2 in the cathode channel ($P_{O_2,CA}$), the mass of carbon support in the cathode catalyst layer per cm^2 (m_C), and the membrane water content (λ). Meanwhile, there are two variables which satisfy algebraic constraints: the membrane phase potential at the anode (ϕ_{AN}) and cell voltage (E_{cell}).

Reaction kinetics.—Three electrochemical reactions take place in the anode



The oxygen reduction reaction Eq. 2 and carbon corrosion reaction Eq. 3 are very small compared with the hydrogen dissociation reaction Eq. 1 in terms of current density (at least 1000-fold difference); nevertheless, such current density corresponds to substantial carbon loss in DEA operation. The carbon corrosion shown in Eq. 3 is generally considered an irreversible reaction in aqueous systems.²⁹ Recent experimental observations^{30–32} have shown carbon loss in the anode, which supports the inclusion of the anode carbon reaction in the model development despite being less severe than the cathode. In the cathode, only the reactions in Eqs. 2 and 3 are considered.

The local distributed current density in the anode i_{AN} is the summation of the main reaction and two partial reactions

$$i_{AN} = i_{H_2,AN} + i_{O_2,AN} + i_{C,AN} \quad [4]$$

For the cathode, there are reactions of oxygen and carbon. The crossover hydrogen is assumed to be completely consumed at the cathode catalyst layer, the accumulation effects are ignored due to the cathode flow-through

$$i_{CA} = i_{O_2,CA} + i_{C,CA} \quad [5]$$

Two algebraic variables in the present model, membrane phase potential at the anode (ϕ_{AN}) and cell voltage (E_{cell}), correspond to the following two equations

$$i_{AN} + i_{CA} = 0 \quad [6]$$

$$i_{fc} = \frac{1}{l} \int_0^l i_{AN} dy \quad [7]$$

Equation 6 represents the local conservation of charge, the total anode local current is equal to the cathode. We assume that the in-plane proton current can be neglected. This assumption is valid due to the low ionic conductivity of the membrane relative to the high electronic conductivity of the current collector.²³ Note that the anodic current (releasing protons) is defined positive and cathodic (consuming protons) negative. Equation 7 specifies the average (apparent) current density drawn from the cell which is a model input. It is important to note that every term in Eqs. 6 and 7 can be expressed as a function of ϕ_{AN} and/or E_{cell} . Thus Eqs. 6 and 7 constitute the constraints for these two variables.

The reaction kinetics of each partial reaction in Eq. 4 are described by the Butler-Volmer relation

$$i_{H_2,AN} = \gamma_{Pt} i_{0,H_2} L_{Pt} \left\{ \frac{P_{H_2}^{CL}}{P_{H_2}^*} \exp \left[\frac{\alpha_{a,H_2} F}{RT} (V_m^{AN} - \phi_{AN} - V_{H_2}^{eq}) \right] - \frac{P_{H_2}^{CL}}{P_{H_2}^*} \exp \left[\frac{-\alpha_{c,H_2} F}{RT} (V_m^{AN} - \phi_{AN} - V_{H_2}^{eq}) \right] \right\} \quad [8]$$

$$P_{H_2}^{CL} = P_{H_2}^{CH} - \frac{i_{H_2,AN} \delta_{GDL} RT}{2FD_{H_2}} \quad [9]$$

$$i_{O_2,AN} = \gamma_{Pt} i_{0,O_2} L_{Pt} \left\{ \frac{P_{V,AN}}{P_{V,AN}^*} \exp \left[\frac{\alpha_{a,O_2} F}{RT} (V_m^{AN} - \phi_{AN} - V_{O_2}^{eq}) \right] - \left(\frac{P_{O_2,AN}}{P_{O_2,AN}^*} \right)^{\beta_{O_2}} \left(\frac{P_{H_2}}{P_{H_2}^*} \right)^{\beta_{H_2}} \exp \left[\frac{-\alpha_{c,O_2} F}{RT} (V_m^{AN} - \phi_{AN} - V_{O_2}^{eq}) \right] \right\} \quad [10]$$

$$i_{C,AN} = \gamma_C i_{0,C} L_C \frac{P_{V,AN}}{P_{V,AN}^*} \exp \left[\frac{\alpha_{a,C} F}{RT} (V_m^{AN} - \phi_{AN} - V_C^{eq}) \right] \quad [11]$$

where γ_* (* = Pt or C) is the active platinum or carbon surface area per unit mass and L_* is the loading of platinum or carbon. ϕ_{AN} is the membrane phase potential at the anode catalyst layer/membrane interface. D_{H_2} is the hydrogen diffusion coefficient in the GDL. Equation 9 represents the effect of hydrogen diffusion through the GDL. Note in Eq. 10, the oxygen partial reaction (water dissociation) depends on both hydrogen and oxygen concentrations, which is different from a normal cathode scenario where hydrogen ion supply is considered sufficient. Also note that ideally, hydrogen ion concentration should be used rather than hydrogen partial pressure, which is a simplification in the model. A similar approach is used in Refs. 33 and 34.

For the cathode, the Butler-Volmer relations are similar

$$i_{O_2,CA} = \varepsilon_C \gamma_{Pt} i_{0,O_2} L_{Pt} \left\{ \frac{P_{V,CA}}{P_{V,CA}^*} \exp \left[\frac{\alpha_{a,O_2} F}{RT} (V_m^{CA} - \phi_{CA} - V_{O_2}^{eq}) \right] - \left(\frac{P_{O_2,CA}^{CL}}{P_{O_2,CA}^*} \right)^{\beta_{O_2}} \left(\frac{P_{H_2}}{P_{H_2}^*} \right)^{\beta_{H_2}} \times \exp \left[\frac{-\alpha_{c,O_2} F}{RT} (V_m^{CA} - \phi_{CA} - V_{O_2}^{eq}) \right] \right\} \quad [12]$$

$$P_{O_2}^{CL} = P_{O_2}^{CH} + \frac{i_{O_2,CA} \delta_{GDL} RT}{4FD_{O_2}} \quad [13]$$

$$i_{C,CA} = \varepsilon_C \gamma_C i_{0,C} L_C \frac{P_{V,CA}}{P_{V,CA}^*} \exp \left[\frac{\alpha_{a,C} F}{RT} (V_m^{CA} - \phi_{CA} - V_C^{eq}) \right] \quad [14]$$

where ε_C is a fraction factor of remaining carbon defined by Eq. 17 to reflect the influences of carbon loss on the reaction kinetics and cell voltage. A similar power factor was also used in Ref. 35 to

account the decreasing rate of carbon corrosion over time, which was observed experimentally.

There are different approaches in modeling the carbon corrosion rate since the mechanism is still not fully understood. The corrosion rate has been shown to drop with time at potential,²⁹ which suggests that the Butler-Volmer equation may not give an accurate prediction of the corrosion rate. This paper focuses on the impact of distributed concentration and reaction rates along the channel associated with DEA operation and presents a way to quantify the carbon/voltage loss. Any model of carbon corrosion, such as the one reviewed in Ref. 29 may be incorporated into our modeling framework. A similar drop in carbon corrosion rate over time is captured by the model through the loss of active platinum sites in Eq. 17, with the parameter ϵ_C . The power factor in Eq. 17 is a tuned parameter which may be studied and tuned in the future.

Cell voltage and local current are used to connect the metal/membrane phase potentials at anode (V_m^{AN}) and cathode (V_m^{CA})

$$V_m^{CA} = V_m^{AN} + E_{cell} + R_{GDL}i_{AN} \quad [15]$$

$$\phi_{CA} = \phi_{AN} - R_{mem}i_{AN} \quad [16]$$

Carbon corrosion.—As carbon corrodes, the electrode becomes thinner and the active catalytic area decreases. In Eqs. 12 and 14, ϵ_C is an effective factor to account for the influence of carbon loss on the cathode reaction kinetics³⁶

$$\epsilon_C(y, t) = \left[\frac{m_C(y, t)}{m_{C,0}} \right]^q \quad [17]$$

where $m_{C,0}$ is the initial carbon loading per unit area and m_C is the carbon mass per unit area. The influences of carbon loss on the effective catalytic area are thus reflected, although a more complicated model of Pt loss (such as dissolution and mitigation^{24,25}) has not been included in this work. Incorporating ϵ_C in Eq. 14 also leads to an asymptotic drop of corrosion current with constant potential, although this drop is associated with Pt loss proportional to the carbon corrosion. Anode carbon loss is negligible compared with cathode (as shown in Fig. 10), therefore the effective factor accounting for carbon loss is not incorporated in Eqs. 8–11.

It should be noted that for Eq. 17, the original model³⁶ uses a power factor $q = 4$ to account for the thinning of electrode (loss of catalytic sites). However, the authors of Ref. 36 state that it is an assumed rather than a fitted or derived parameter. In this work, the power factor q is reduced to 1.5, which produces more consistent modeling results with our experimental observations.³⁷ A factor of 4 leads to high over-estimate of the cell voltage decay over time as compared with the experimental results.

The local carbon loss m_C is related to the carbon reaction rate at cathode $i_{C,CA}$

$$\frac{\partial m_C}{\partial t} = -\frac{M_C i_{C,CA}}{4F} \quad [18]$$

where F is the Faraday constant and M_C is the molar mass of carbon.

Along-channel mass transport.—The time dependent composition in the anode is modeled using Stefan-Maxwell equations for a quaternary system (H_2 , O_2 , N_2 , H_2O) and solved by spatial discretization and numerical time integration. The model describes the mass conservation (for the gas phase only) including convection, diffusion, and source terms in the anode channel

$$\frac{P_{AN}}{RT} \frac{\partial n_i}{\partial t} = -\frac{\partial}{\partial y} (J_i + n_i N_t) + r_i \quad [19]$$

for $i = [1, 2, 3, 4] = [N_2, H_2O, O_2, H_2]$, where N_t is the total convective gas flux, J_i is the diffusive flux, and r_i denotes the source terms (reactive and/or crossover fluxes per unit channel height). All fluxes discussed in this paper have a unit of $\text{mol m}^{-2}\text{s}^{-1}$. Only three of the four components are independent in this modeling framework. We

choose to model the mole fractions of nitrogen, n_{N_2} , water vapor, n_{H_2O} and oxygen, n_{O_2} , as our dynamic states. The hydrogen molar fraction can be calculated from the other three since $\sum n_i = 1$. The anode pressure, P_{an} , is assumed to be constant since it is set by an upstream pressure regulator during the DEA operation.

The causal formulation for the quaternary Stefan-Maxwell diffusive fluxes can be summarized as

$$J_i = -\frac{P_{AN}}{RT\psi(n)} W \frac{\partial n_i}{\partial y} \quad [20]$$

where ψ is a scalar function of the species molar fractions and W is a 4 by 4 coefficient matrix (refer to Ref. 38).

Assuming the outlet flow is given by $N_t(l) = N_{out}$, then conservation of total mass (gas mixture) allows solving of Eq. 19 for $N_t(y)$. Since $\sum J_i = 0$ by definition, the equation for mass conservation can be written as

$$\frac{\partial N_t}{\partial y} = \sum r_i \quad [21]$$

Then the convective flux along the channel can be found by

$$N_t(y) = N_t(l) + \int_y^l [r_{H_2,ret}(\tilde{y}) + r_{H_2,crs}(\tilde{y}) + r_{N_2,crs}(\tilde{y}) + r_{H_2O,crs}(\tilde{y}) + r_{H_2O,ret}(\tilde{y}) + r_{O_2,crs}(\tilde{y}) + r_{O_2,ret}(\tilde{y})] d\tilde{y} \quad [22]$$

The expressions for $r_{H_2,ret}$, $r_{N_2,crs}$, $r_{H_2O,crs}$ are given below without further explanation since details are available in Ref. 11

$$r_{H_2,ret} = \frac{i_{H_2,AN}}{2Fh_{ch,an}} \quad [23]$$

$$r_{N_2,crs} = -K_{N_2} \frac{P_{N_2,CA} - P_{N_2,AN}}{\delta_{mb}h_{ch,an}} \quad [24]$$

$$r_{H_2O,crs} = -\frac{\lambda_{CA} - \lambda_{AN}}{R_{mb}h_{ch,an}} + n_d \frac{i_{AN}}{Fh_{ch,an}} \quad [25]$$

where R_{mb} is the resistance to membrane transport and n_d is the electro-osmotic drag coefficient.

Given the fast reaction kinetics of crossover hydrogen at the cathode catalyst layer, the partial pressure of hydrogen at cathode is assumed to be zero. Thus the hydrogen crossover flux is a function of hydrogen pressure at anode P_{H_2} only

$$r_{H_2,crs} = K_{H_2} \frac{P_{H_2}^{PCL}}{\delta_{mb}h_{ch,an}} \quad [26]$$

in which the permeance of hydrogen through the membrane K_{H_2} is a function of membrane water content and temperature³⁹

$$K_{H_2} = (0.29 + 2.2f_v) \times 10^{-14} \exp \left[\frac{E_{H_2}}{R} \left(\frac{1}{T_{ref}} - \frac{1}{T} \right) \right] \quad [27]$$

Similarly for $r_{O_2,crs}$, $r_{O_2,ret}$ and $r_{H_2O,ret}$

$$r_{O_2,crs} = -K_{O_2} \frac{P_{O_2,CA}^{PCL} - P_{O_2,AN}}{\delta_{mb}h_{ch,an}} \quad [28]$$

$$r_{O_2,ret} = -\frac{i_{O_2,AN}}{4Fh_{ch,an}} \quad [29]$$

$$r_{H_2O,ret} = \frac{i_{O_2,AN}}{2Fh_{ch,an}} \quad [30]$$

where $P_{O_2,CA}/P_{O_2,AN}$ is the partial pressure of oxygen in the cathode/anode and δ_{mb} is the thickness of membrane. For simplicity it is assumed that oxygen only accumulates in the gas phase and not in

the ionomer phase due to the large volume difference between the channel and membrane. The expression for $i_{O_2,AN}$, the anode partial current density of oxygen reaction, is given by Eq. 10. The permeance of oxygen through membrane K_{O_2} ($\text{mol Pa}^{-1} \text{m}^{-1} \text{s}^{-1}$) in Eq. 28 is correlated with temperature and membrane water content³⁹

$$K_{O_2} = \beta_K (0.11 + 1.9f_v) \times 10^{-14} \exp\left[\frac{E_{O_2}}{R} \left(\frac{1}{T_{ref}} - \frac{1}{T}\right)\right] \quad [31]$$

where β_K is a scale factor for tuning the oxygen crossover flux, $E_{O_2} = 20 \text{ kJ/mol}$, and f_v is the volume fraction of water in membrane defined by

$$f_v = \frac{\lambda V_w}{V_m + \lambda V_w} \quad [32]$$

where V_w is the molar volumes of water in membrane, and the molar volume of dry membrane (equivalent weight by density) $V_m = EW/P_{mb,dry}$.

In the cathode, the material balance for oxygen is established considering diffusion, convection, reaction and crossover. The nitrogen partial pressure can be then obtained since the cathode system pressure is assumed to be constant. The oxygen partial pressure in the cathode channel is the last state in the model

$$\begin{aligned} \frac{1}{RT} \frac{\partial P_{O_2,CA}}{\partial t} = & -\frac{D_{O_2}}{RT} \frac{\partial^2 P_{O_2,CA}}{\partial y^2} + \frac{1}{RT} \frac{\partial (P_{O_2,CA} u_{ca,in})}{\partial y} - \frac{i_{O_2,CA}}{4Fh_{ch,ca}} \\ & + \frac{K_{H_2} P_{H_2}^{CL}}{2\delta_{mb} h_{ch,ca}} + \frac{r_{O_2,crs}}{h_{ch,ca}} \end{aligned} \quad [33]$$

where D_{O_2} is the Fickian diffusivity of O_2 , h the channel depth and $u_{ca,in}$ the gas velocity at cathode inlet (assumed constant along the channel for simplicity)

$$u_{ca,in} = \frac{SR_{ca} i_{fc} l_{ca} RT (w_{ch,ca} + w_{rib,ca})}{4FSP_{O_2,CA,in} h_{ch,ca} w_{ch,ca}} \quad [34]$$

where SR_{ca} is the stoichiometry ratio in the cathode and S the total MEA area.

Note that Eqs. 19 and 33 correspond to the four states in the model (n_{N_2,H_2O,O_2} and $P_{O_2,CA}$), and Eq. 33 is coupled with Eq. 12.

The six dynamic states together with two algebraic variables are solved simultaneously using Matlab ODE15s solver. The central difference scheme is used for discretizing spatial derivatives. The parameter values of the present model are summarized in Table I.

Model Parameterization

There are three tunable parameters: i_{0,O_2} , β_{H_2} and β_K (see Eqs. 10, 12 and 31). i_{0,O_2} and β_{H_2} impact the local kinetics of the oxygen reaction in the anode and β_K impacts the oxygen crossover rate from cathode to anode. It is found that $i_{0,C}$ has very limited influence on the species concentration and cell voltage, although it directly affects the carbon corrosion rate. We do not have sufficient experimental data for tuning $i_{0,C}$ at this time. The value of $i_{0,C}$ is taken from Ref. 23. Refer to Table II for the tunable ranges for i_{0,O_2} , β_{H_2} , β_K . The tuned i_{0,O_2} is close to the one in Ref. 23.

Experimental setup.—The experimental data of species molar fractions was collected using a gas chromatograph.¹¹ The setup is schematically shown in Fig. 4. A heated capillary tube was inserted into the last anode channel near the edge of the cell (3 cm from the bottom corner), it was then connected to an electrically actuated six-port rotational valve. A sample valve placed downstream from the six-port valve, once open, allowed for filling of the sample loop. After a sample was collected the six-port valve was rotated to close, and the high pressure carrier gas helium pushed the sample into the GC for analysis. The sample valve was

Table I. Geometrical, physical and operating parameters.

Quantity	Value
Geometrical parameters	
Active MEA area, S	50 cm ²
Anode channel depth, $h_{ch,an}$	0.18 cm
Cathode channel depth, $h_{ch,ca}$	0.10 cm
Cathode channel/Rib width, $w_{ch/rib,ca}$	0.07/0.08 cm
Channel length, l	7.27 cm
Membrane thickness, δ_{mb}	25 μm
GDL thickness, δ_{GDL}	300 μm
Physical parameters	
Catalyst loading, L_{Pt}	$0.3/2 \times 10^{-3} \text{ g cm}^{-2}$
Electrochemical area of Pt, γ_{Pt}	$6 \times 10^5 \text{ cm}^2 \text{ g}^{-1}$
Carbon loading, L_C	$2 \times 10^{-3} \text{ g cm}^{-2}$
Electrochemical area of carbon, γ_C	$6 \times 10^6 \text{ cm}^2 \text{ g}^{-1}$
Diffusion coefficient of hydrogen, D_{H_2}	$0.76 \text{ cm}^2 \text{ s}^{-1}$
Diffusion coefficient of oxygen, D_{O_2}	$0.23 \text{ cm}^2 \text{ s}^{-1}$
Concentration parameter for hydrogen, β_{H_2}	1.2
Concentration parameter for oxygen, β_{O_2}	1.0
Anodic transfer coefficient for hydrogen reaction, α_{a,H_2}	1.0
Cathodic transfer coefficient for hydrogen reaction, α_{c,H_2}	1.0
Anodic transfer coefficient for oxygen reaction, α_{a,O_2}	0.6
Cathodic transfer coefficient for oxygen reaction, α_{c,O_2}	1.0
Anodic transfer coefficient for carbon corrosion, $\alpha_{a,C}$	0.25
Exchange current density of hydrogen reaction, i_{0,H_2}	$1.7 \times 10^{-3} \text{ A cm}^{-2}$
Exchange current density of oxygen reaction, i_{0,O_2}	$2.6 \times 10^{-9} \text{ A cm}^{-2}$
Exchange current density of carbon corrosion, $i_{0,C}$	$2.5 \times 10^{-10} \text{ A cm}^{-2}$
Equilibrium potential for hydrogen reaction, $V_{H_2}^{eq}$	0 V
Equilibrium potential for oxygen reaction, $V_{O_2}^{eq}$	1.23 V
Equilibrium potential for carbon corrosion, V_C^{eq}	0.21 V
Anode metal potential, V_m^{AN}	0 V
Scale factor for oxygen crossover, β_K	0.72
Initial carbon loading per unit MEA area, $m_{C,0}$	0.002 g cm^{-2}
Anode reference pressure $P_{i,AN}^*$, $i = [H_2, O_2, \text{vapor}]$	$1.2755 \times 10^5 \text{ Pa}$
Cathode reference pressure $P_{i,CA}^*$, $i = [O_2, \text{vapor}]$	$1.2355 \times 10^5 \text{ Pa}$
Number of meshes in numerical computation, N	51
Operating parameters	
Cell temperature, T	50°C
Inlet pressure at anode, P_{AN}	4.5 psig
System pressure at cathode, P_{CA}	4 psig
Duration of a cycle, t	1020 s

opened for 1 s, during which $\sim 300 \mu\text{l}$ of gas was removed from the anode channel. A second Solenoid Valve, shown in the lower right hand corner of Fig. 4, was used to purge all of the N_2 from the cell. The flow rate during the purge was approximately 0.5 SLPM, and the purge duration was around 1 s in order to ensure that all of the accumulated water and nitrogen are removed from the channels. More details about the setup and experimental results can be found in Ref. 11.

The experimental results for comparison were obtained under the following conditions: the anode is dead ended and the cathode is flow through. The operating conditions for each case are indicated in the captions of the figure. i : current density in A cm^{-2} , T : temperature in °C, SR : cathode stoichiometry, RH : relative humidity of cathode supply). The anode/cathode pressure (absolute) is $1.2755 \times 10^5/1.2355 \times 10^5 \text{ Pa}$ for all cases. These operating conditions are also used to obtain the simulation results. The selected portions of the data to validate the model (Figs. 5–7) start from $t_0 = 57495 \text{ s}$, 73786 s and 82940 s , respectively (see Ref. 11 for the entire data set). For each case, the membrane water content and local current density profiles at three locations (0.2, 0.5 and 0.9

Table II. Tuned parameters.

Quantity	Range for tuning	Value
Exchange current density of oxygen reaction, i_{0,O_2}	$10^{-5} - 10^{-12} \text{ A cm}^{-2}$ ^{a,b,c}	$2.6 \times 10^{-9} \text{ A cm}^{-2}$
Concentration parameter for hydrogen reaction, β_{H_2}	0.5–1.5	1.2
Scale factor for oxygen crossover, β_K	0.5–2.0	0.72
Power factor for remaining carbon, q	0–4.0 ^d	1.5

^aReference 7^bReference 9^cReference 23^dReference 36

fractional channel length) are plotted. The fractional channel length of 0.9 corresponds to the GC sample location, where the experimental data of molar fractions were collected.

Calibration results.—The simulated along-channel species concentrations agree well with the experimental data. In all three cases the model slightly over-estimates the cell voltage. This may be attributed to the influence of liquid water on the mass transport loss in calculating the cell voltage, which is not captured by the present model. In cases 2 and 3, there exists discrepancies of nitrogen molar fraction at ~ 2000 s, which might be due to the liquid water plugging in the channel end regions. Nitrogen does not participate in any reaction, however its transport can still be influenced by water plugging. Liquid water may block the outlet purge flow and prevent gas from entering the sample loop, resulting in measurement error. As time evolves over a cycle, the model predicts uneven local current distribution and membrane water content illustrated by the bottom plots of Fig. 7. The best agreement between simulation and experiments are observed for case 2 with current load of 0.4 A cm^{-2} . This result may be attributed to the relatively uniform local current and water distribution under this operating condition. Thus, the same operating conditions are used for discussion of the simulation results in the next section. The

most uneven membrane water content distribution is observed in case 1, which is the result of high current load and low cathode inlet RH.

Simulation Results

In this section, we use the conditions of case 2 to investigate the spatiotemporal variation of species concentration and partial current density. The operating conditions are as follows: the temperature is fixed at 50°C , and the total current drawn from the cell is 20A (0.4 A cm^{-2}). The dead ended anode is supplied with dry ($\text{RH}=0$) H_2 and the cathode humidified air ($\text{RH}=0.90$) at a stoichiometry of 3. The tuned values in Table II and other parameter values in Table I are used for simulation. Every 1020 s, the solenoid valve at the anode outlet opens for 1 s to recover the cell voltage by releasing the accumulated nitrogen and water. The results reported in this section are obtained in one complete cycle from a fresh start following a purge (100% hydrogen in anode) up until the next scheduled purge at ~ 1020 s. Note that in the simulation, complete hydrogen starvation does not occur even in the channel end, because the anode is purged every 1020 s. This purge schedule is consistent with the validated case 2 shown in Fig. 6, in which the system is purged before severe fuel depletion occurs.

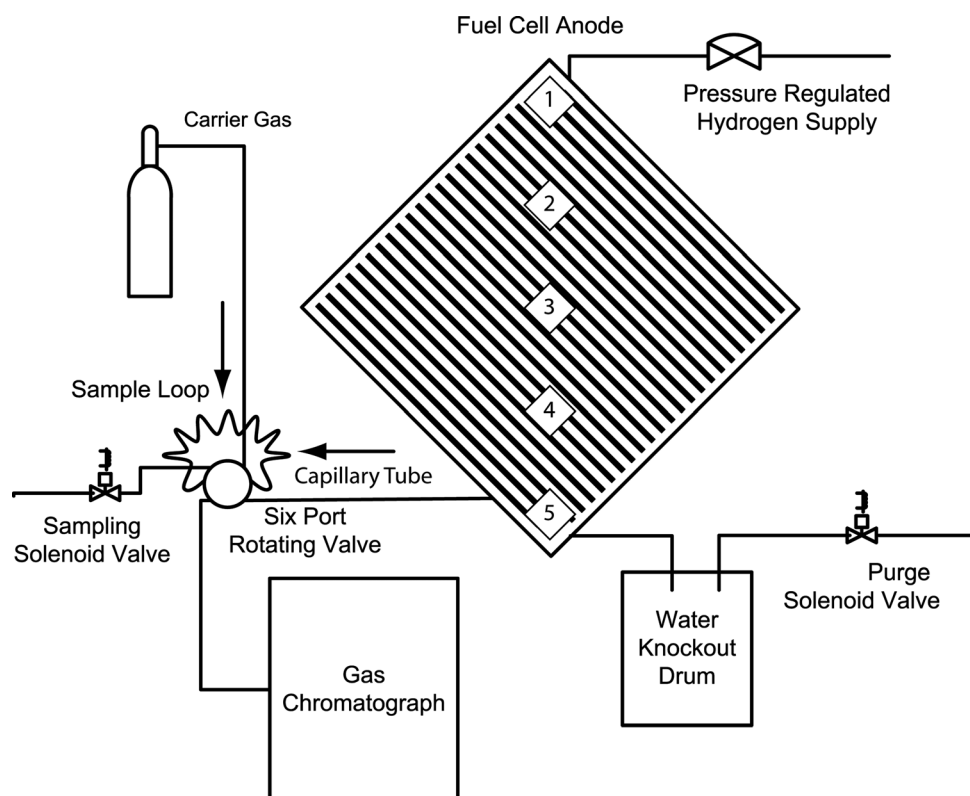


Figure 4. Illustration of the GC setup with six-port rotating valve. The marked locations 1–5 (from inlet to outlet) designate the positions of MEA samples which were used for SEM diagnosis, refer to Ref. 37 for more details of the degradation test.

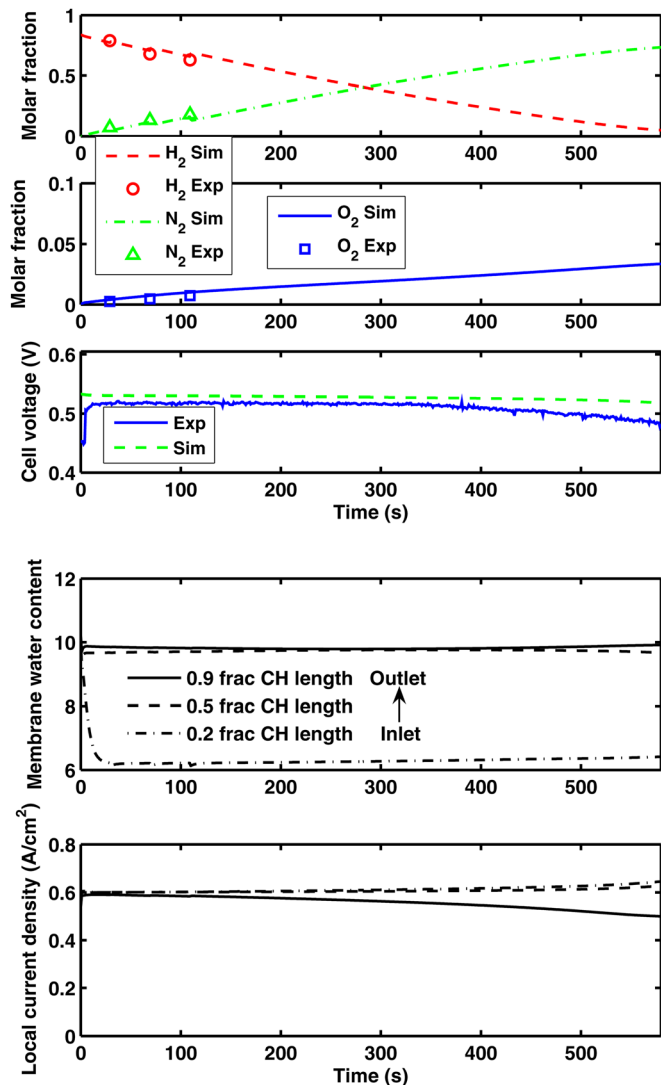


Figure 5. (Color online) Top: Comparison of case 1: $t_0 = 57495$ s, OPC: i0.6-T60-SR2-RH75. For molar fractions, markers are from experimental measurements and lines from simulation results. For cell voltage, blue solid line is from experimental measurements and green dashed line from simulation results. Bottom: Model predicted membrane water content and local current evolutions at selected channel locations (solid line represents GC sample location) for case 1.

Species concentration.—The simulation results for the species molar fractions in both anode and cathode at selected times (100 s, 500 s and 1000 s) are shown in Fig. 8. At $t = 1000$ s, severe hydrogen depletion ($< 5\%$) is observed within the bottom 20% of the channel in the anode, as hydrogen consumed in reaction is displaced by gases and liquid water which cross over from the cathode. These effects have been discussed in our previous work.^{3,11} In this paper the oxygen crossover, accumulation and its effect on carbon corrosion are emphasized. Overall, the molar fraction of oxygen is low ($< 5\%$) and it increases along the channel due to convection. There are two sources for oxygen in the anode: crossover from the cathode and water dissociation in the anode. Figure 9 shows both the reactive and crossover fluxes of oxygen in the anode at selected times. The negative value of reactive fluxes indicates that the net effect of $O_2 + 4H^+ + 4e^- \leftrightarrow 2H_2O$ is moving forward and generating water (see also Fig. 10b). As indicated by the absolute values of reactive/crossover fluxes, the average rate of oxygen crossover is higher than oxygen consumption in the anode. The simulation therefore suggests that crossover oxygen reduces the rate of water dissociation,

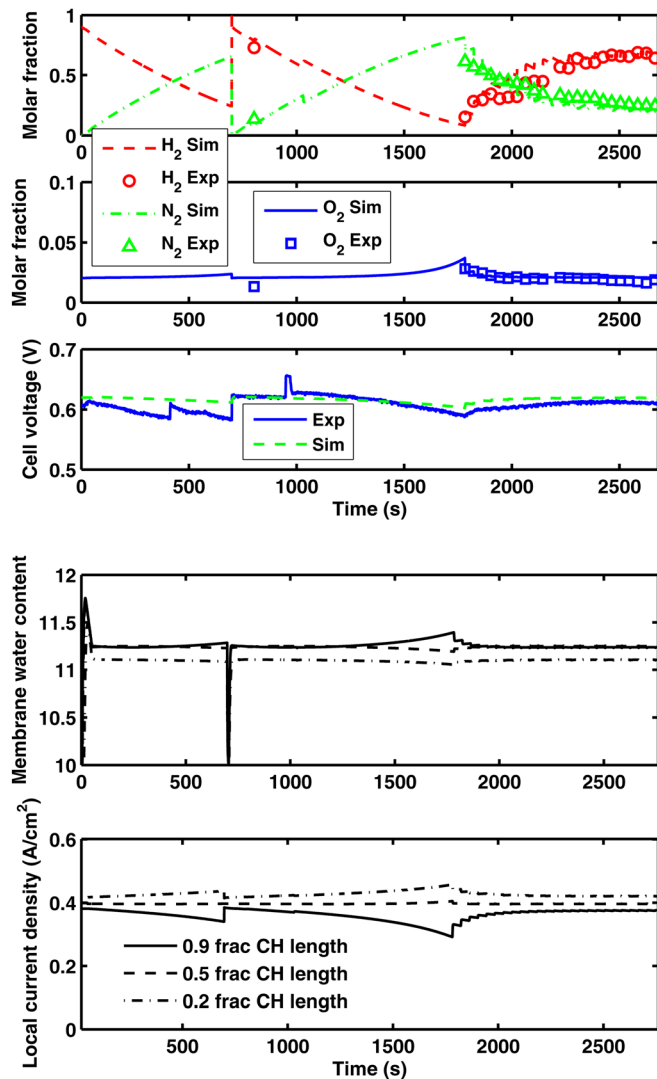


Figure 6. (Color online) Top: Comparison of case 2: $t_0 = 73786$ s, OPC: i0.4-T50-SR3-RH90. For molar fractions, markers are from experimental measurements and lines from simulation results. For cell voltage, blue solid line is from experimental measurements and green dashed line from simulation results. Bottom: Model predicted membrane water content and local current evolutions at selected channel locations (solid line represents GC sample location) for case 2.

because the additional oxygen moves the equilibrium towards the direction of water generation. This increases the rate of carbon corrosion in the anode, since hydrogen ions are further consumed in the region of fuel depletion. However, the calculated carbon corrosion rate in the anode is still negligible, as shown in Fig. 10.

Examining the cathode molar fraction plot (subplot (d) in Fig. 8) we observe that the oxygen profile is almost linear at $t = 100$ s, being a result of relatively uniform local reaction rates. At $t = 1000$ s, the curve shows non-linear behavior due to the uneven local current.

The partial current density evolutions are shown in Fig. 10. As expected, the current density of hydrogen reaction is decreasing with time at the channel end region, because accumulated nitrogen and water displace hydrogen. The local current profile becomes more uneven as time evolves. The magnitude of $i_{C,AN}$ ($\sim 10^{-7}$ A cm^{-2}) from the simulation indicates that carbon corrosion at the anode is negligible. The cathode carbon corrosion rate is much higher, see Fig. 12 and discussion therein.

Interfacial potentials.—The variation of membrane phase potential in the anode is a direct result of the presence of oxygen. In the

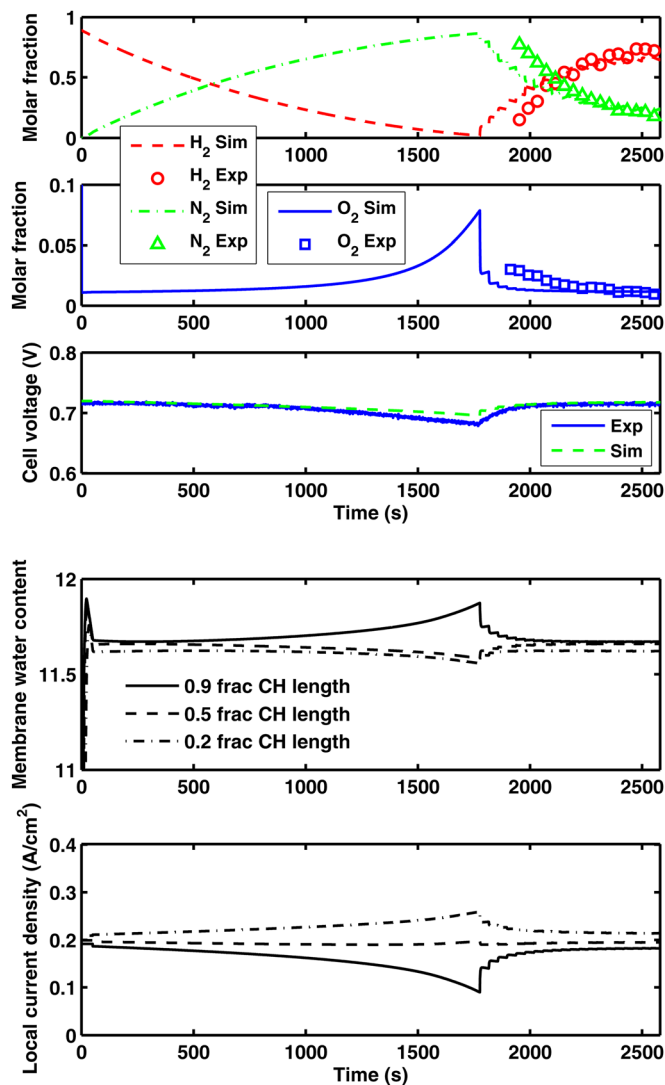


Figure 7. (Color online) Top: Comparison of case 3: $t_0 = 82940$ s, OPC: i0.2-T50-SR3-RH95. For molar fractions, markers are from experimental measurements and lines from simulation results. For cell voltage, blue solid line is from experimental measurements and green dashed line from simulation results. Bottom: Model predicted membrane water content and local current evolutions at selected channel locations (solid line represents GC sample location) for case 3.

model, the membrane phase potential at anode/cathode enters into the Butler-Volmer expression for the kinetic of each partial reaction (Eqs. 8–11). Figure 11 shows the evolution of both anode and cathode interfacial potentials. The anode interfacial potential is equal to the absolute value of membrane phase potential at the anode, whereas the cathode potential depends on the overall cell voltage (see Eqs. 15 and 16). During normal operation, with sufficient hydrogen supply everywhere, ϕ_{AN} should be slightly negative (very close to zero). After 1000 s, ϕ_{AN} decreases to approximately -0.1 V in the end region. The decrease of ϕ_{AN} along the channel promotes the water dissociation and carbon corrosion reactions at the anode. The drop is continuous over the whole channel length, as opposed to the sudden drop due to a H_2/O_2 boundary induced during start-up/shutdown.⁹ Similar hydrogen molar fraction and ϕ_{AN} profiles, featuring a gradual drop, were reported by Weber,⁴⁰ except that the end region was completely out of fuel.

Membrane phase potential at the cathode (Eq. 16) is not plotted since the potential drop through membrane is only ~ 0.01 V. The interfacial potential at the cathode, $V_m^{CA} - \phi_{CA}$, is shown in Fig. 11. This interfacial potential directly determines the carbon corrosion

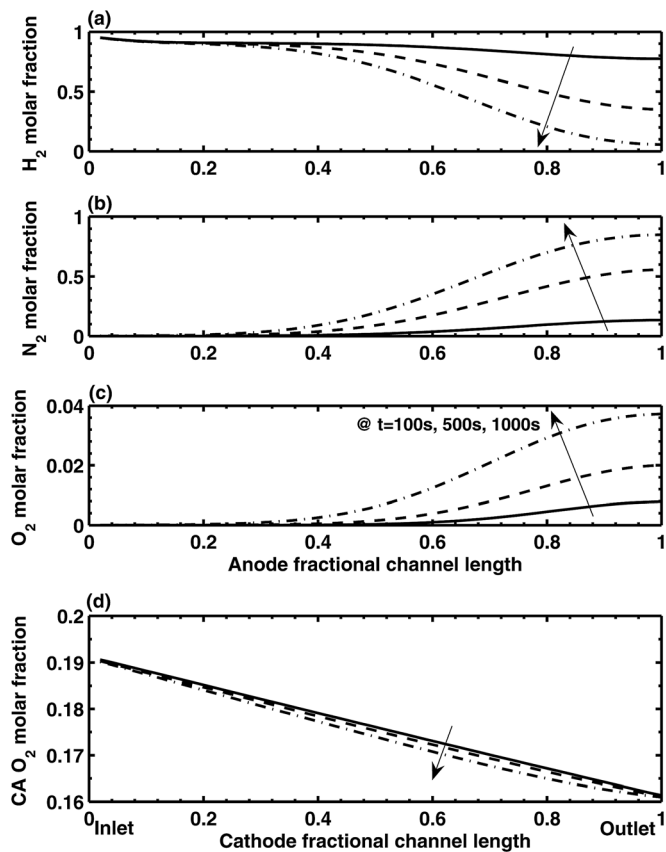


Figure 8. Molar fraction evolutions of (a)hydrogen/(b)nitrogen/(c)oxygen in the anode channel and (d) oxygen in the cathode channel.

rate at the cathode. The predicted interfacial potentials are not as large as in start-up/shutdown case⁹ for two reasons. First, the cell voltage in an operating cell is lower than the open circuit voltage due to thermodynamic losses. Therefore, the resulting metal phase potential at the cathode is normally less than 1 V (see Eq. 15). The cell voltage is decreasing during a cycle of DEA operation, which offsets the effect of the decreasing membrane phase potential.

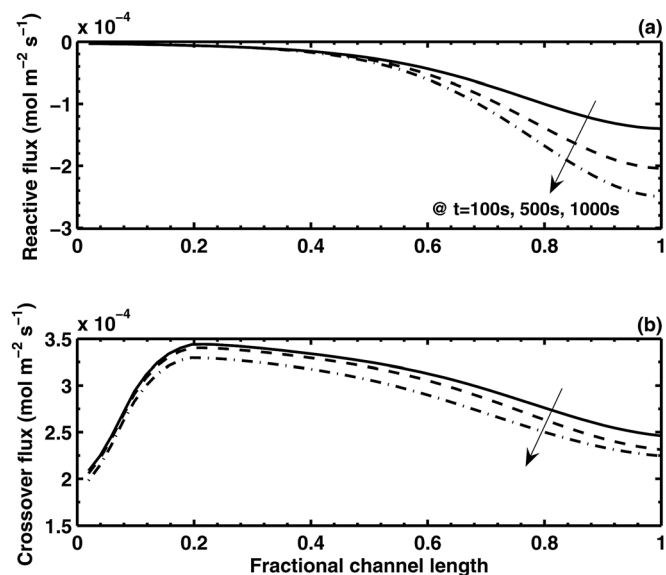


Figure 9. Evolutions of (a) reactive and (b) crossover fluxes of oxygen in the anode.

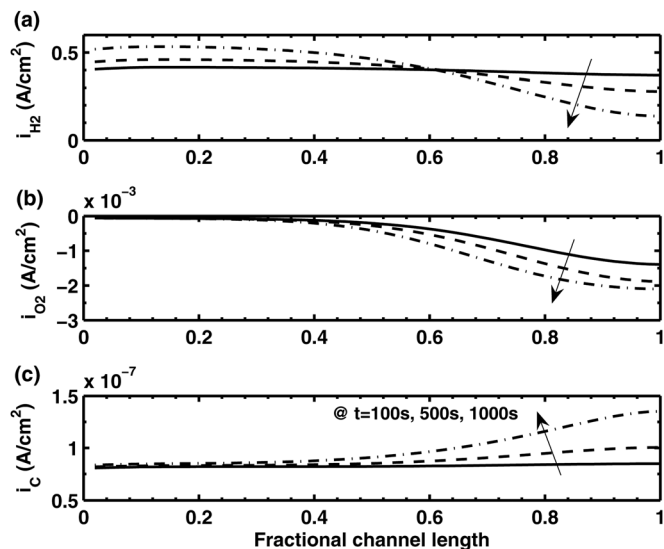


Figure 10. Anode partial current density evolutions of (a) hydrogen, (b) oxygen and (c) carbon reactions.

Therefore, a cell under operation, either with flow through or DEA, would normally experience much less severe carbon corrosion compared with an idle one in which H_2/O_2 boundary builds up. The second reason is that in simulation the anode is purged before complete fuel starvation. A postponed purge may lead to higher cathode interfacial potential and carbon corrosion rate.

Carbon corrosion.—The predicted local cathode corrosion rates in selected cycles are plotted in Fig. 12a. As hydrogen becomes depleted in the anode end region, the cathode end region endures the highest corrosion rate, which is caused by the increased cathode interfacial potential in this region (see Fig. 11). The cathode carbon corrosion rate at the end region is twice as large as the inlet right before the purge. However, when the hydrogen depletion is mild, the corrosion rate is much more uniform. The carbon corrosion rate predicted by the model is higher than other rates found in the literature,^{35,41} but the carbon corrosion rate in the model has not been rig-

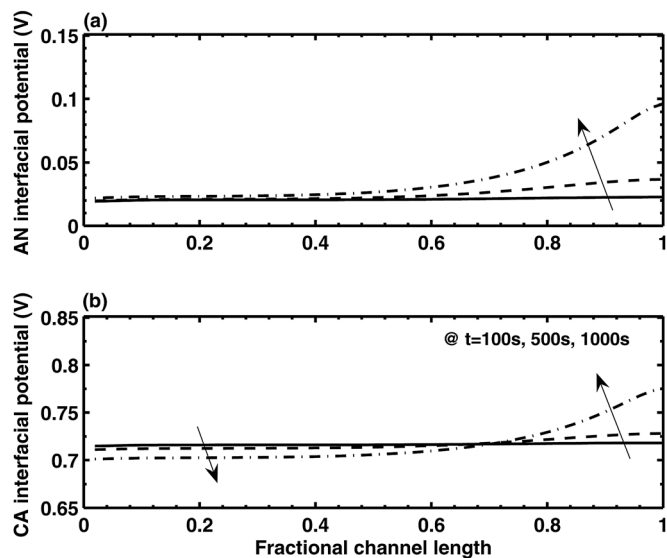


Figure 11. Evolutions of (a) anode and (b) cathode interfacial potentials. The cathode interfacial potential decreases near the channel inlet because of the increase current density in this region (Fig. 10a). The increase at the outlet is due to the anode side potential shift in the same region.

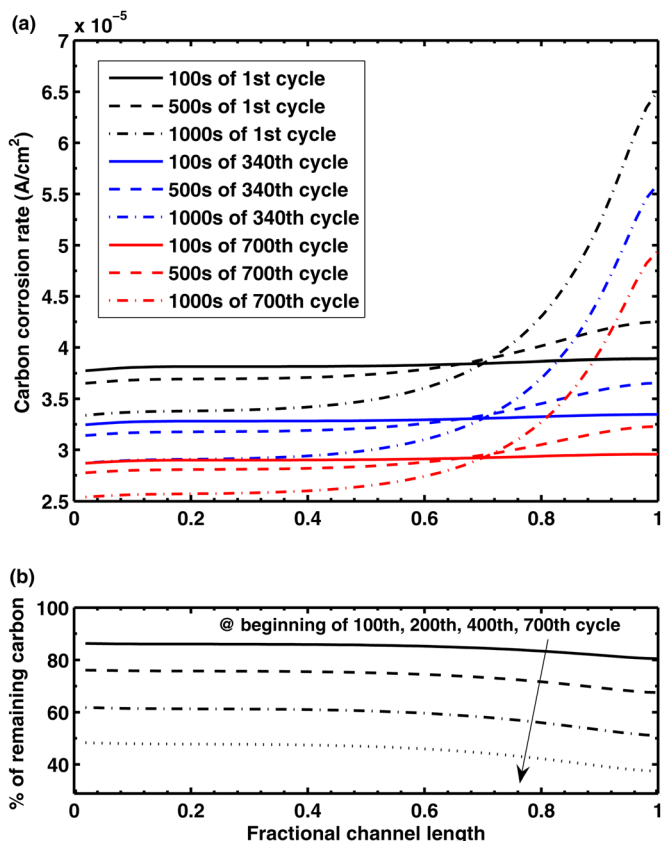


Figure 12. (Color online) (a) Evolution of the cathode carbon corrosion rate in the 1st, 340th and 700th cycle, respectively. The overall corrosion rate decreases with time due to the loss of catalytic sites. (b) The remaining carbon evaluated locally by the percentage of initial loading after 100, 200, 400 and 700 cycles, respectively.

orously tuned. It can be tuned by the parameters q in Eq. 17, $i_{0,C}$ and $\alpha_{a,C}$ in Eq. 14 once more data are collected, particularly the measurement of CO_2 concentration at the cathode.

The relationship between reactant distribution and carbon corrosion during DEA operation is captured by this physics based and tunable model. Since the connection between carbon loss and voltage drop over time is included in the model, it can be used to develop control laws to prolong cell life. The percentage of remaining carbon is shown in Fig. 12b. The initial carbon loading is assumed to be uniform. The uneven corrosion rate leads to increased carbon loss along the length of the channel. The non-uniformity of remaining carbon along the channel is not as severe as the local corrosion rate before the purge because the local corrosion rate does not increase until a nitrogen blanketing front in the anode channel begins to develop. If the cell could be purged before the corrosion rate at the end region starts to spike, then the catalyst durability may be greatly improved.

The local percentage of remaining carbon at the beginning of 100th cycle is consistent with our experimental measurement of the aged MEA shown in Fig. 13. The data shown in Fig. 13 also confirm that the anode carbon corrosion is negligible compared with cathode. The trend at location 2 seems to be inconsistent with the model prediction. This could be attributed to measurement error and/or other degradation mechanisms not included in the model. More experimental data are being collected to clarify the spatial variability, and initial results are reported in Ref. 37. Nevertheless, the carbon corrosion rate can be independently tuned since it has negligible influence on the species transport, because the current density of carbon corrosion is at least 1000 times smaller than the main reaction (Eq. 1).

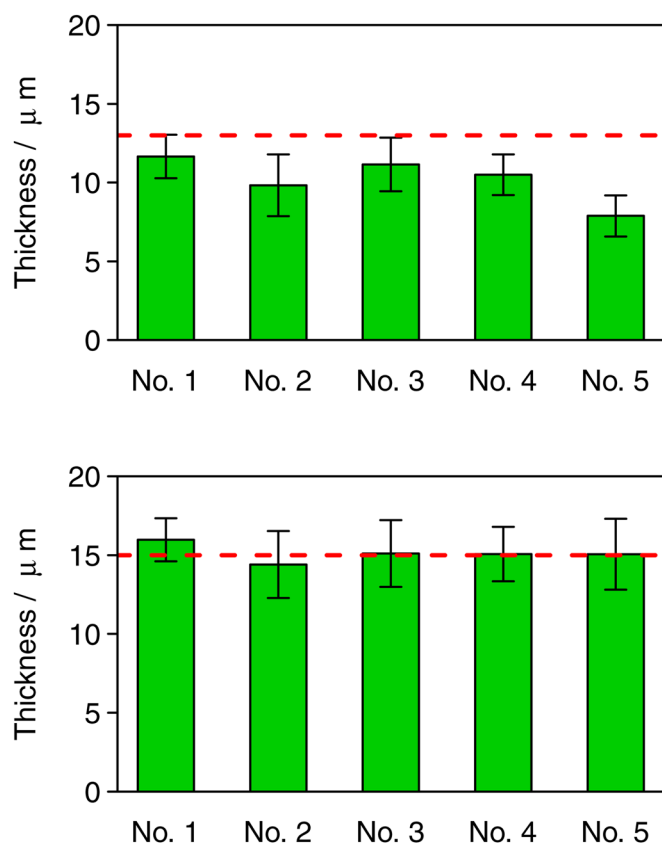


Figure 13. (Color online) Measured electrode thickness of the aged MEA, top: cathode and bottom: anode. The dotted red lines denote the original thickness of electrodes at cathode and anode. Numbers 1–5 refer to the sample positions shown in Fig. 4. More details of the degradation test are available in Ref. 37.

The model can be also used to examine the influence of initial Pt/C loadings in the catalyst layer on the corrosion rate and cell voltage performance. The detailed information of Pt/C ratio is not released by our MEA supplier Ion Power, Inc. However, a typical ratio 1 ($2/2 \text{ mg cm}^{-2}$) and a reduced ratio 0.15 ($0.3/2 \text{ mg cm}^{-2}$) are used in the parametric study. Figure 14a shows that increasing Pt/C ratio from 0.15 to 1 leads to about 10% more carbon loss after 700 cycles. This suggests that increasing the initial Pt loading may not be decremental for long term DEA performance.

Another effect from carbon loss and reduced catalytic area is the reduced cell voltage over time, which is shown in Fig. 14b. Mathematically the reduced cell voltage leads to larger absolute value of the cathodic exponential term in Eq. 12 so that the reduced exchange current density can be compensated to maintain the required current. The modeling results indicate that the cell voltages show decay of $\sim 0.035 \text{ V}$ over 700 cycles for Pt/C ratio 0.15 and 0.04 V for Pt/C ratio 1. Such decay is expected to be observed repeatedly in ongoing experiments, and it may become an effective diagnostic tool for carbon corrosion in DEA operation. Note that other degradation effects such as Pt agglomeration⁴² also affect the cell voltage, however they are neglected here.

Conclusions

In this work, we developed an along-channel model to predict the carbon corrosion in DEA operation. The membrane phase potential in the DEA mode exhibits a gradual drop along the channel, as compared to the start-up/shutdown case where the sharp boundary between fuel and oxidant develops in the anode channel. Therefore different modeling equations for the gas transport in the channels are required to describe the corrosion behavior. This model captures

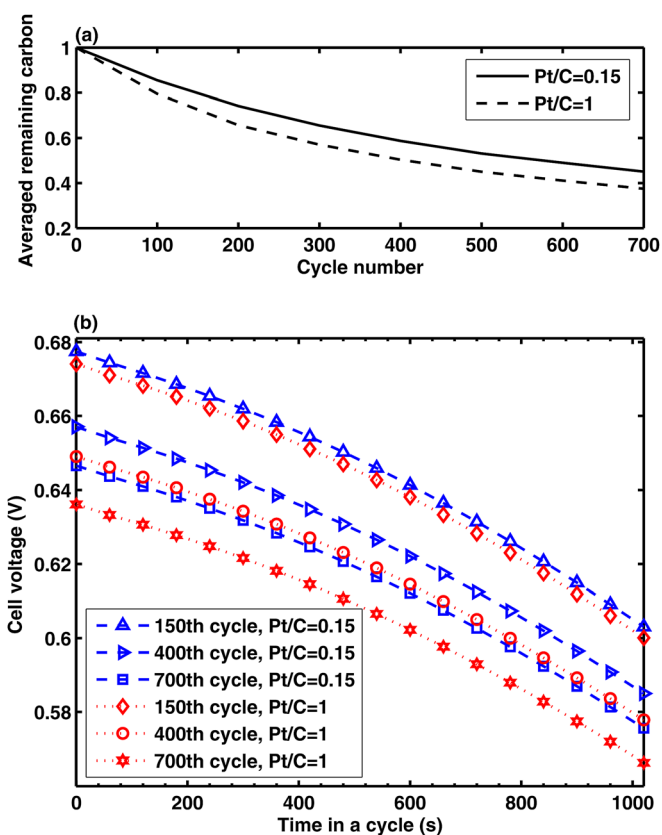


Figure 14. (Color online) (a) The remaining carbon averaged over the whole channel evaluated by the percentage of initial loading after each cycle. (b) The model predicted performance decay of cell voltage within a DEA operation cycle due to the carbon loss. Two different initial Pt/C ratios (0.15 and 1) are used to generate these figures.

the effect of nitrogen accumulation and current density distribution on carbon loss. The carbon loss is related to a decrease in the number of active catalytic sites via a power law correlation of the amount of carbon remaining in the catalyst layer. The model predicts the non-recoverable voltage loss during DEA operation associated with decrease in carbon corrosion rate as the catalyst layer is thinned.

Experimental data including GC samples and cell voltage are compared with the model prediction and demonstrate satisfactory agreement at low current loads. A snapshot of the temporal evolution right before the purge, shows that the carbon corrosion rate at the end channel region is at least twice as large as the inlet region. The time evolving terminal cell voltage directly affects the interfacial potential at the cathode. Fortunately, the gradual voltage decay, associated with higher local hydrogen current density, during DEA operation reduces the cathode carbon corrosion rate.

In the future the model can be improved by including the effects of liquid water, Pt sintering, mass transport limitations due to changes in catalyst layer composition, and membrane degradation. The addition of these factors may improve the model prediction of non-recoverable voltage drop over time, particularly at high operating current. The present model captures the effect of nitrogen accumulation and current density distribution on carbon loss. The carbon loss is related to a decrease in the number of active catalytic sites via a power correlation of the amount of carbon remaining in the catalyst layer. The model predicts the non-recoverable voltage loss during DEA operation associated with decrease in carbon corrosion rate as the catalyst layer is thinned. The voltage prediction can be used to develop better purge scheduling and closed loop estimation. If the cell is purged before the corrosion rate at the end region starts to spike, then the catalyst durability may be greatly improved. Purge

scheduling that accounts for carbon corrosion through a well calibrated model can balance the hydrogen loss occurring during a purge with the durability issues associated with delaying a purge event. Future work includes collecting data on cell voltage and CO₂ evolution to further validate and tune the actual carbon corrosion rate.

Acknowledgments

This work is funded by the National Science Foundation through CBET-0932509 and Ford Motor Company.

List of Symbols

i , A cm ⁻²	Local current density
i_{fc} , A cm ⁻²	Average current density
k	Number of cycles
t , s	Time
m , g cm ⁻²	Mass per unit area
l , cm	Channel length
w , cm	Channel width
h , cm	Channel depth
n	Molar fraction
r , mol m ⁻³ s ⁻¹	Reactive/Crossover flux (through membrane) per unit depth
q	Tunable power factor for remaining carbon
u , m s ⁻¹	Gas velocity
$C/H_2/N_2/O_2/V(H_2O)$	Carbon/Hydrogen/Nitrogen/Oxygen/Vapor
D , m ² s ⁻¹	Diffusivity
E_{cells} , V	Cell voltage
F	Faraday's constant
L , g cm ²	Catalyst/Carbon loading
M	Molar fraction
N_T , mol m ⁻² s ⁻¹	Total gas flux (along channel)
J , mol m ⁻² s ⁻¹	Diffusive flux (along channel)
K , mol m ⁻¹ s ⁻¹ Pa ⁻¹	Gas permeance
T , K	Temperature
P , Pa	Pressure
R , J K ⁻¹ mol ⁻¹	Gas constant
S , cm ²	Area
V_m , V	Metal phase potential
W	Coefficient matrix in Stefan-Maxwell diffusion

Greek

α	Transfer coefficient
β	Tunable parameter for hydrogen reaction/oxygen crossover
γ , cm ² g ⁻¹	Electrochemical area
λ	Membrane water content
Φ , V	Membrane phase potential
ψ	Scaler function in Stefan-Maxwell diffusion
ε	Effective factor for remaining carbon

Shorthand/Subscript/Superscript

AN	Anode
CA	Cathode
CH	Flow Channel
GDL	Gas Diffusion Layer
CL	Catalyst Layer
MEM	Membrane
OPC	Operating condition
$RH = P_v/P_{sat}$	Relative humidity
sat	Saturation

References

- P. Mocoteguy, F. Druart, Y. Bultel, S. Besse, and A. Rakotondrainibe, *J. Power Sources*, **167**, 349 (2007).
- D. McKay, J. Siegel, W. Ott, and A. Stefanopoulou, *J. Power Sources*, **178**, 207 (2008).
- J. Siegel, D. McKay, A. Stefanopoulou, D. Hussey, and D. Jacobson, *J. Electrochem. Soc.*, **155**, B1168 (2008).
- J. Benziger, *AIChE J.*, **55**, 3034 (2009).
- E. A. Muller, F. Kolb, L. Guzzella, A. G. Stefanopoulou, and D. A. McKay, *J. Fuel Cell Sci. Technol.*, **7**, 0210131 (2010).
- J. Benziger, E. Chia, E. Karnas, J. Moxley, C. Teuscher, and I. G. Kevrekidis, *AIChE J.*, **50**, 1889 (2004).
- R. Borup, J. Meyers, B. Pivovar, Y.-S. Kim, R. Mukundan, N. Garland, D. Myers, M. Wilson, F. Garzon, D. Wood, et al., *Chem. Rev.*, **107**, 3904 (2007).
- J. Wu, X. Yuan, J. Martin, H. Wang, J. Zhang, J. Shen, S. Wu, and W. Merida, *J. Power Sources*, **184**, 104 (2008).
- C. Reiser, L. Bregoli, T. Patterson, J. Yi, J. Yang, M. Perry, and T. Jarvi, *Electrochem. Solid-State Lett.*, **8**, A273 (2005).
- L. Roen, C. Paik, and T. Jarvi, *Electrochem. Solid-State Lett.*, **7**, A19 (2004).
- J. Siegel, S. Bohac, A. Stefanopoulou, and S. Yesilyurt, *J. Electrochem. Soc.*, **157**, B1081 (2010).
- J. Siegel, A. Stefanopoulou, G. Ripaccioli, and S. Di Cairano, *The Control Handbook, Control System Applications*, 2nd ed., W. S. Levine, Editor, CRC Press, London (2010).
- J. Hu, P. Sui, S. Kumar, and N. Djilali, *Electrochim. Acta*, **54**, 5583 (2009).
- J. H. Ohs, U. Sauter, S. Maass, and D. Stolten, *J. Power Sources*, **196**, 255 (2011).
- H. Tang, Z. Qi, M. Ramani, and J. Elter, *J. Power Sources*, **158**, 1306 (2006).
- A. Young, J. Stumper, and E. Gyenge, *J. Electrochem. Soc.*, **156**, B913 (2009).
- T. W. Patterson and R. M. Darling, *Electrochem. Solid-State Lett.*, **9**, A183 (2006).
- Q. Shen, M. Hou, D. Liang, Z. Zhou, X. Li, Z. Shao, and B. Yi, *J. Power Sources*, **189**, 1114 (2009).
- K. H. Lim, H.-S. Oh, S.-E. Jang, Y.-J. Ko, H.-J. Kim, and H. Kim, *J. Power Sources*, **193**, 575 (2009).
- D. Condit and R. Breault, U.S. Pat. 6,635,370 (2003).
- T. Bekkedahl, L. Bregoli, R. Breault, E. Dykeman, J. Meyers, T. Patterson, T. Skiba, C. Vargas, D. Yang, and J. Yi, U.S. Pat. 6,913,845 (2005).
- Y. D. Decker, J. B. Benziger, E. Kimball, and I.G. Kevrekidis, *Chem. Eng. Sci.*, **65**, 2399 (2010).
- J. Meyers and R. Darling, *J. Electrochem. Soc.*, **153**, A1432 (2006).
- R. Darling and J. Meyers, *J. Electrochem. Soc.*, **150**, A1523 (2003).
- R. Darling and J. Meyers, *J. Electrochem. Soc.*, **152**, A242 (2005).
- D. Curtin, R. Lousenberg, T. Henry, P. Tangeman, and M. Tisack, *J. Power Sources*, **131**, 41 (2004).
- V. Mittal, H. Kunz, and J. Fenton, *J. Electrochem. Soc.*, **154**, B652 (2007).
- F. Rong, C. Huang, Z.-S. Liu, D. Song, and Q. Wang, *J. Power Sources*, **175**, 699 (2008).
- K. Kinoshita, *Carbon—Electrochemical and Physicochemical Properties*, John Wiley & Sons, New York (1988).
- Z. Liu, L. Yang, Z. Mao, W. Zhuge, Y. Zhang, and L. Wang, *J. Power Sources*, **157**, 166 (2006).
- Z. Liu, B. Brady, R. Carter, B. Litterer, M. Budinski, J. Hyun, and J. D. Muller, *J. Electrochem. Soc.*, **155**, B979 (2008).
- D. Liang, Q. Shen, M. Hou, Z. Shao, and B. Yi, *J. Power Sources*, **194**, 874 (2009).
- Y. Wang and C.-Y. Wang, *J. Electrochem. Soc.*, **152**, A445 (2005).
- K. Jiao and X. Li, *Electrochim. Acta*, **54**, 6876 (2009).
- W. Gu, P. T. Yu, R. N. Carter, R. Makharia, and H. A. Gasteiger, *Modeling and Diagnostics of Polymer Electrolyte Fuel Cells, Modern Aspects of Electrochemistry 49*, U. Pasaogullari and C.-Y. Wang, Editors, Springer Science+Business Media, LLC, New York (2010).
- A. A. Franco and M. Gerard, *J. Electrochem. Soc.*, **155**, B367 (2008).
- T. Matsuura, J. Siegel, J. Chen, and A. Stefanopoulou, in *Proceeding of ASME 2011 5th International Conference on Energy Sustainability & 9th Fuel Cell Science, Engineering and Technology Conference*, accepted.
- N. Amundson, T.-W. Pan, and V. Paulsen, *AIChE J.*, **49**, 813 (2003).
- R. Ahluwalia and X. Wang, *J. Power Sources*, **171**, 63 (2007).
- A. Weber, *J. Electrochem. Soc.*, **155**, B521 (2008).
- P. T. Yu, W. Gu, R. Makharia, F. T. Wagner, and H. A. Gasteiger, *ECS Trans.*, **3**(1), 797 (2006).
- Y. Shao, R. Kou, J. Wang, V. V. Viswanathan, J. H. Kwak, J. Liu, Y. Wang, and Y. Lin, *J. Power Sources*, **185**, 280 (2008).